

Supporting Information for

Surface-Alloyed Nanoporous Zinc as Reversible and Stable Anodes for High-Performance Aqueous Zinc-Ion Battery

Huan Meng^{1, #}, Qing Ran^{1, #}, Tian-Yi Dai^{1, #}, Hang Shi¹, Shu-Pei Zeng¹, Yong-Fu Zhu¹, Zi Wen¹, Wei Zhang¹, Xing-You Lang^{1, 2, *}, Wei-Tao Zheng¹, Qing Jiang^{1, *}

¹Key Laboratory of Automobile Materials (Jilin University), Ministry of Education, School of Materials Science and Engineering, and Electron Microscopy Center, Jilin University, Changchun 130022, P. R. China

²State Key Laboratory of Automotive Simulation and Control, Jilin University, Changchun 130022, P. R. China

Huan Meng, Qing Ran and Tian-Yi Dai have contributed equally to this work

*Corresponding authors. E-mail: xylang@jlu.edu.cn (Xing-You Lang), jiangq@jlu.edu.cn (Qing Jiang)

Supplementary Figures

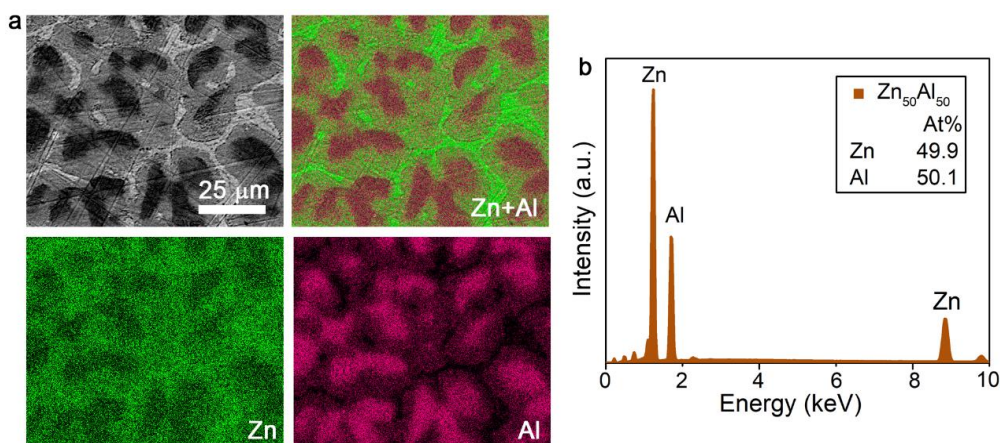


Fig. S1 (a) Low-magnification SEM backscattered electron image of $Zn_{50}Al_{50}$ precursor alloy and the corresponding EDS elemental mapping of Zn and Al, which are in green and purple, respectively. (b) EDS spectrum of $Zn_{50}Al_{50}$ precursor alloy

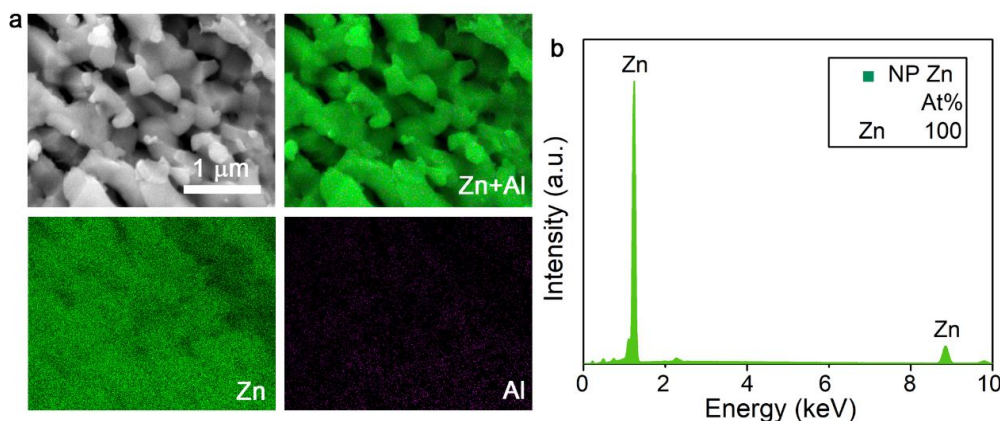


Fig. S2 (a) Low-magnification SEM backscattered electron image of as-prepared nanoporous Zn sheets and the corresponding EDS elemental mapping of Zn and Al, which are in green and purple, respectively. (b) EDS spectrum of as-prepared nanoporous Zn sheets

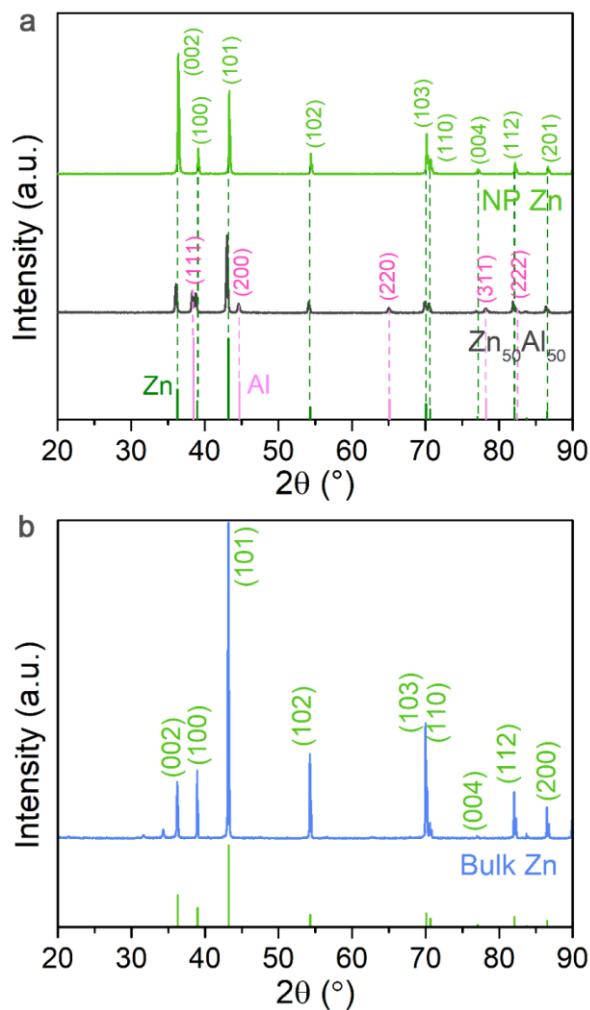


Fig. S3 (a) XRD patterns of Zn₅₀Al₅₀ precursor alloy and as-dealloyed nanoporous Zn in N₂-purged 1 M KOH solution. Therein, the nanoporous Zn is primarily composed of (002) plane. (b) XRD patterns of bulk Zn foil, which is primarily composed of (101) crystal plane

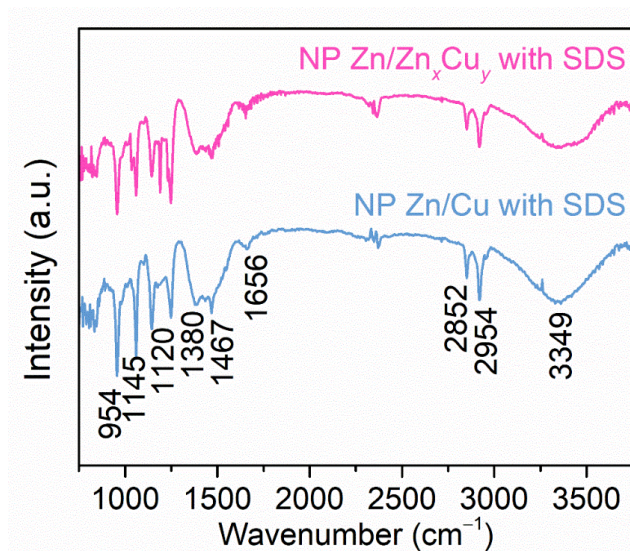


Fig. S4 FTIR spectra of SDS grafted on nanoporous Zn/Cu and Zn_xCu_y/Zn. The peak at 954 cm⁻¹ corresponds to the asymmetric stretching vibration of C-O-S of SDS. The peaks at 1380 and 1467 cm⁻¹ are symmetric and asymmetric deformation vibrations of -CH₃, respectively. The peaks at 2852 and 2954 cm⁻¹ are due to -CH₂ symmetric and asymmetric stretching

vibrations respectively. In addition, the peaks at 1656 and 3349 cm^{-1} are assigned to the characteristic peaks of water molecules adsorbed on the surface. Compared with those of SDS grafted on nanoporous Zn/Cu, the peaks of the SDS on nanoporous $\text{Zn}_x\text{Cu}_y/\text{Zn}$ in the range of 700-1500 cm^{-1} blue shift, indicating the charge transfer between the hydrophilic polar headgroup of SDS and the Zn_xCu_y alloy. Meanwhile, in the FTIR spectrum of nanoporous $\text{Zn}_x\text{Cu}_y/\text{Zn}$ with SDS, new peaks corresponding to S=O stretching vibration and CF_3 asymmetric stretching vibration in OTF^- appear at 1033 and 1189 cm^{-1} , respectively, due to the adsorption of OTF^- on the electrode surface during the cycling process. The peak of the two curves at 1145 cm^{-1} may be attributed to the deviation of SO_4^{2-} characteristic peak of SDS head at 1220 cm^{-1}

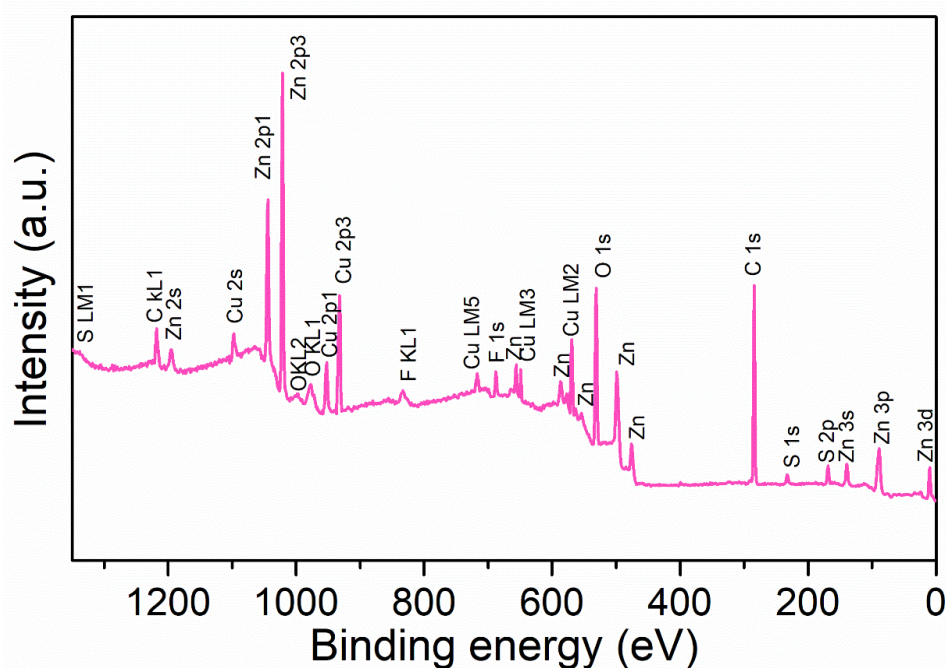


Fig. S5 XPS survey spectrum of nanoporous $\text{Zn}_x\text{Cu}_y/\text{Zn}$ electrode

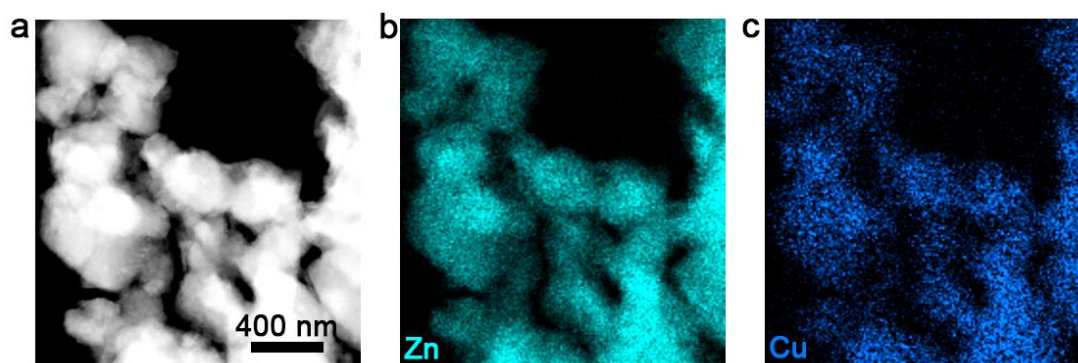


Fig. S6 (a) STEM image and the corresponding (b) Zn and (c) Cu EDS elemental mapping of nanoporous $\text{Zn}_x\text{Cu}_y/\text{Zn}$ electrode, with Zn in cyan and Cu in blue

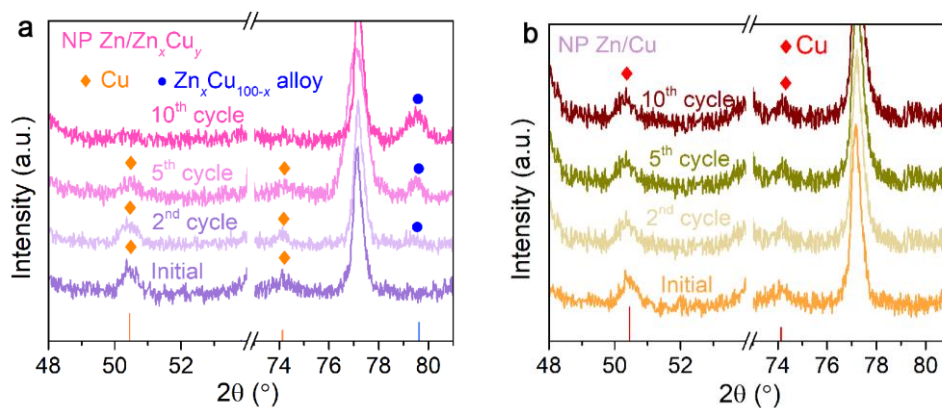


Fig. S7 (a) Typical XRD patterns of nanoporous Zn_xCu_y/Zn , of which the Zn_xCu_y alloy shell in-situ forms on Zn core via surface alloying of Cu and Zn with the assistance of SDS during Zn stripping/plating processes. (b) Typical XRD patterns of nanoporous Cu/Zn, which keeps the initial Cu/Zn structure during Zn stripping/plating processes without the assistance of SDS

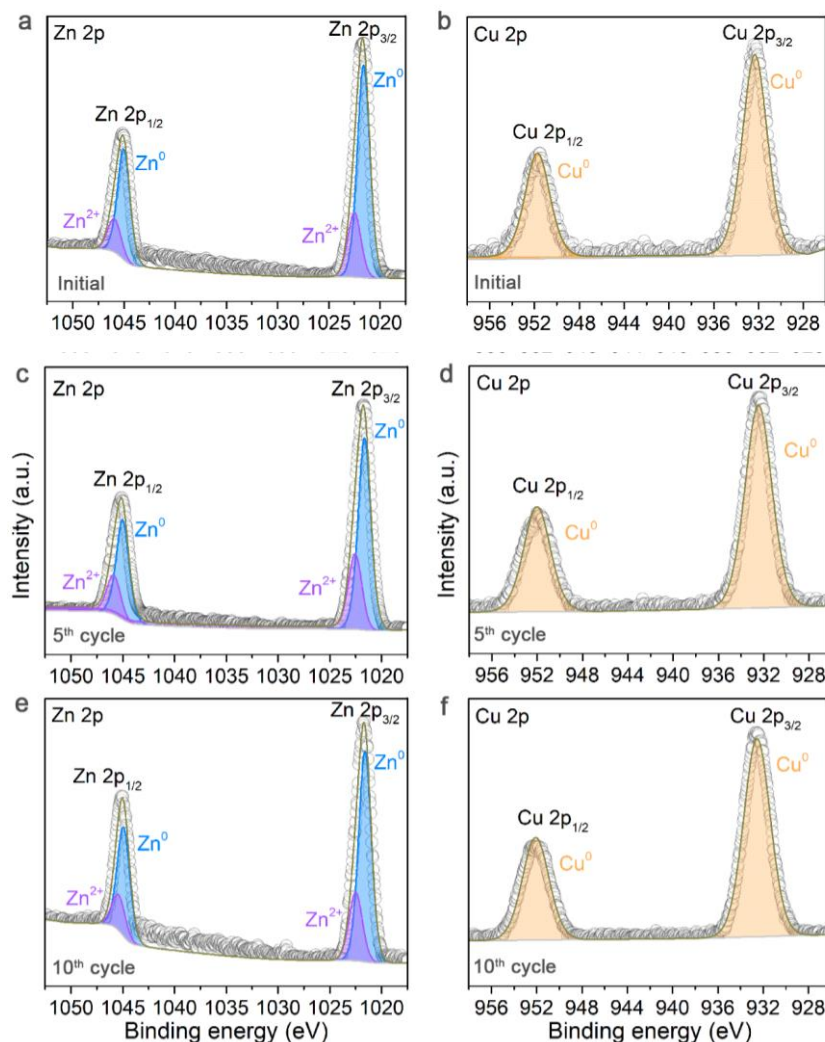


Fig. S8 High-resolution XPS spectra of Zn 2p of nanoporous Zn_xCu_y/Zn during the Zn stripping/plating for 0 (a), 5 (c) and 10 (e) cycles e in 1 M $Zn(OTF)_2$ aqueous electrolyte with SDS additive. High-resolution XPS spectra of Cu 2p of nanoporous Zn_xCu_y/Zn during the Zn stripping/plating for 0 (b), 5 (d) and 10 (f) cycles in 1 M $Zn(OTF)_2$ aqueous electrolyte with SDS additive

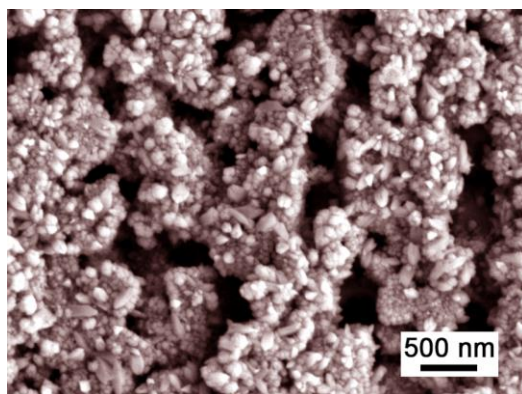


Fig. S9 Representative SEM image of nanoporous Cu/Zn after Zn stripping/plating for 10 cycles in 1 M Zn(OTF)₂ without SDS additive

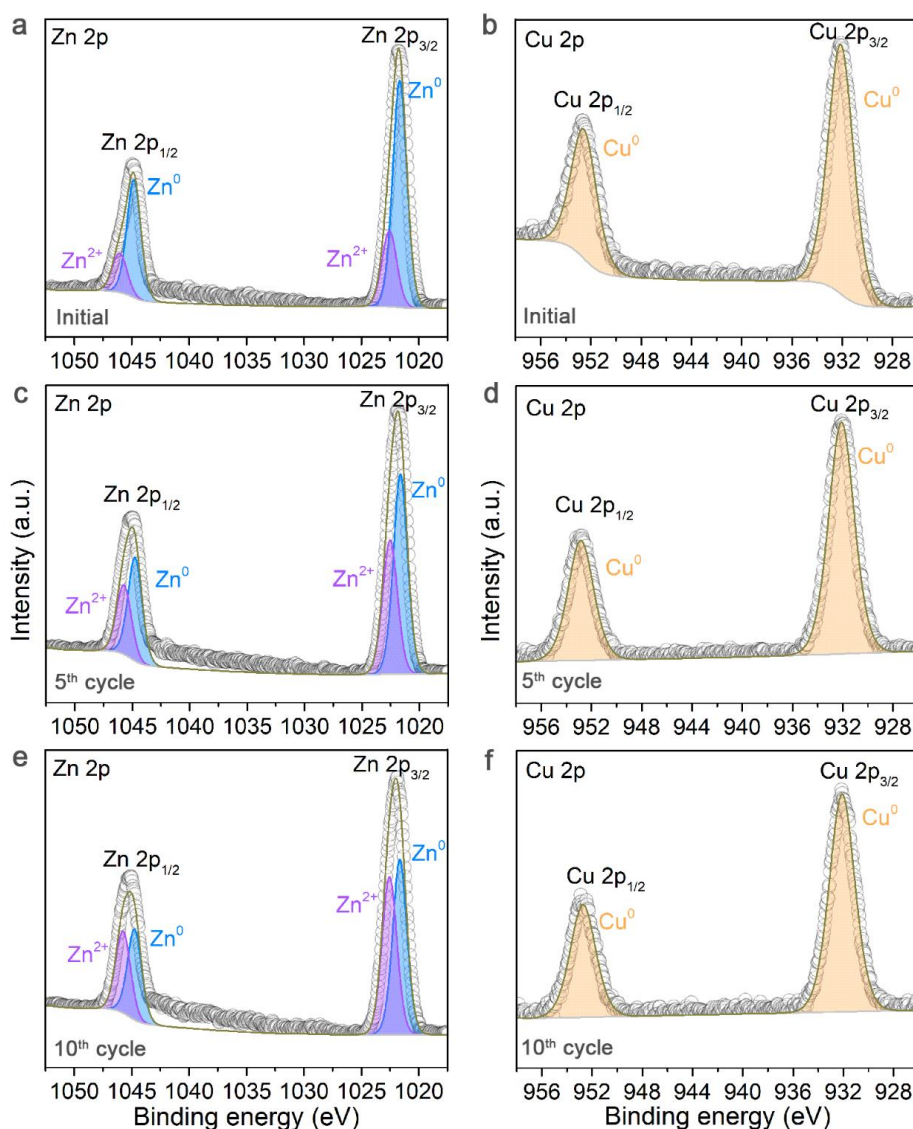


Fig. S10 (a, c, e) High-resolution XPS spectra of Zn 2p of nanoporous Cu/Zn during the Zn stripping/plating for 0 (a), 5 (c) and 10 cycles (e) in 1 M Zn(OTF)₂ aqueous electrolyte without SDS additive. **(b, d, f)** High-resolution XPS spectra of Cu 2p of nanoporous Cu/Zn during the Zn stripping/plating for 0 (b), 5 (d) and 10 (f) cycles in 1 M Zn(OTF)₂ aqueous electrolyte without SDS additive

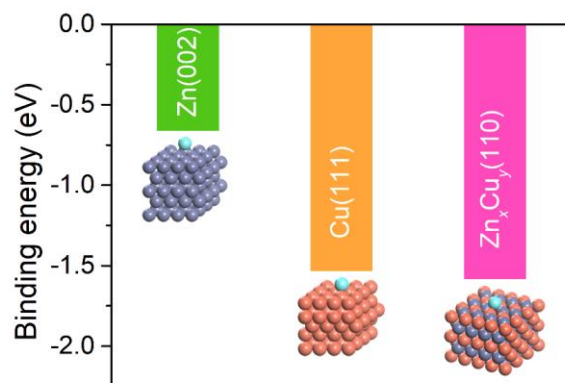


Fig. S11 Comparison of binding energy for Zn atom deposition on Zn(002), Cu(111) and $Zn_xCu_y(110)$ surfaces. Insets: Configurations of one Zn atom deposition on the Zn(002), Cu(111) and $Zn_xCu_y(110)$ surfaces

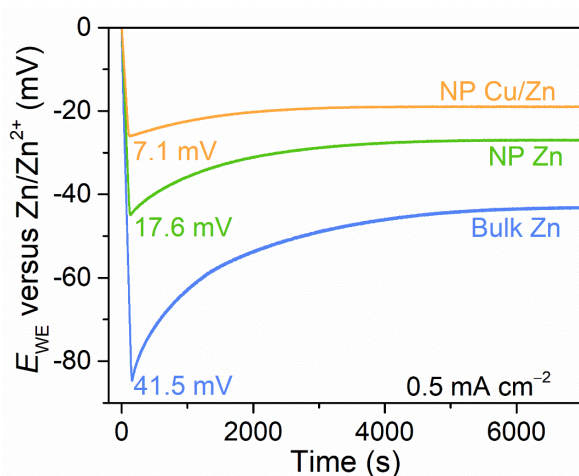


Fig. S12 Comparisons of voltage profiles for galvanostatic Zn deposition on nanoporous Cu/Zn and Zn electrodes, as well as bulk Zn at 0.5 mA cm^{-2}

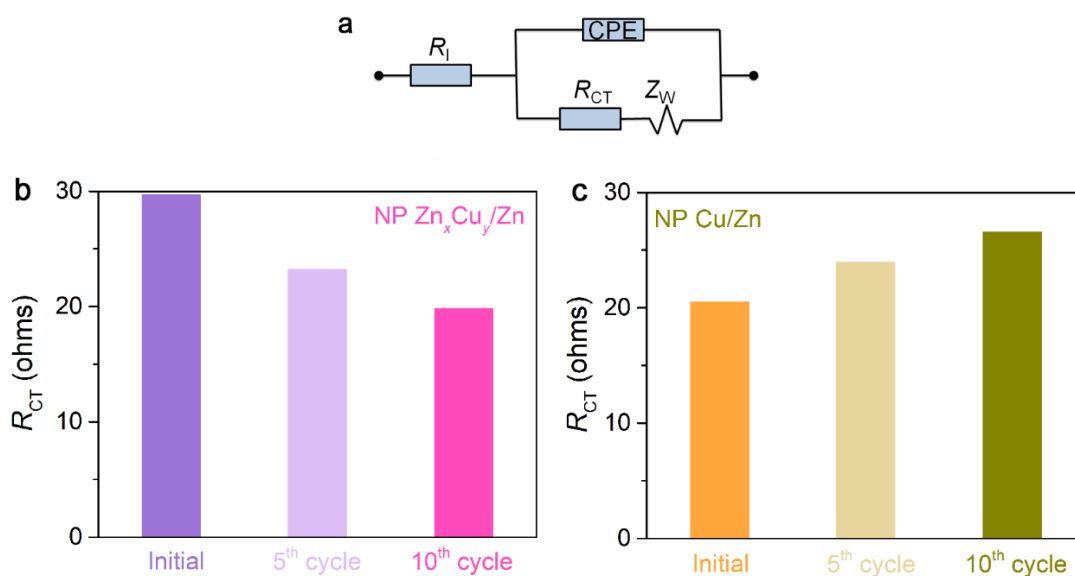


Fig. S13 (a) The equivalent circuit with the general descriptors: the intrinsic resistance of both electrolyte and electrode (R_1), the charge transfer resistance (R_{CT}), the constant phase element (CPE) and the slope of the inclined line at flow frequencies corresponding to the Warburg resistance (Z_w). **(b)** Comparison of R_{CT} values for nanoporous Zn_xCu_y/Zn during the Zn stripping/plating for 0, 5 and 10 cycles in 1 M $Zn(OTf)_2$ aqueous electrolyte with SDS additive.

(c) Comparison of R_{CT} values for nanoporous Cu/Zn during the Zn stripping/plating for 0, 5 and 10 cycles in 1 M Zn(OTF)₂ aqueous electrolyte without SDS additive

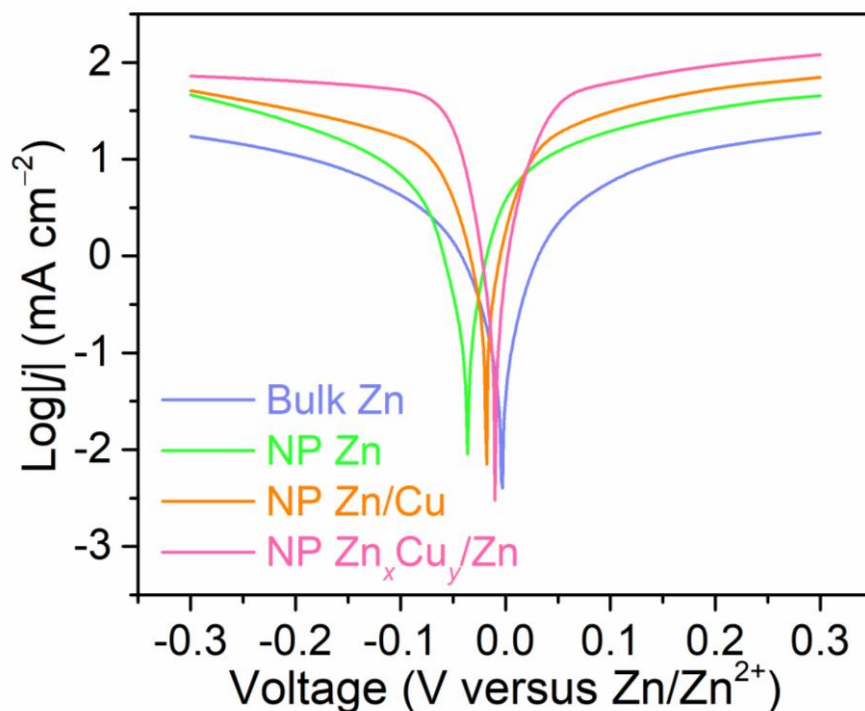


Fig. S14 Tafel polarization curves of nanoporous Zn_xCu_y/Zn, nanoporous Cu/Zn, nanoporous Zn and bulk Zn electrodes

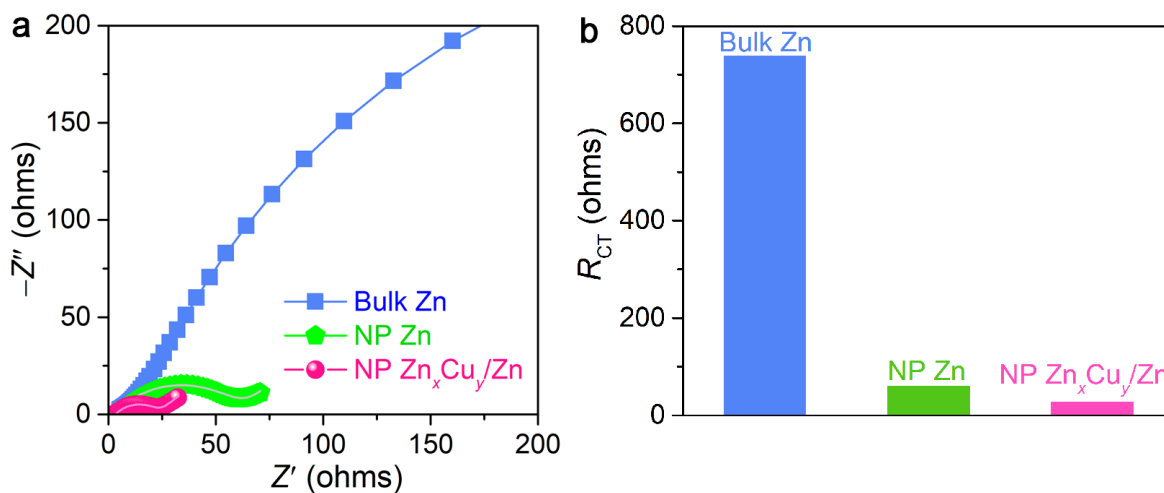


Fig. S15 (a) EIS spectra of symmetric cells based on nanoporous Zn_xCu_y/Zn, nanoporous Zn and bulk Zn electrodes. (b) Comparison of R_{CT} values for nanoporous Zn_xCu_y/Zn, nanoporous Zn and bulk Zn electrodes

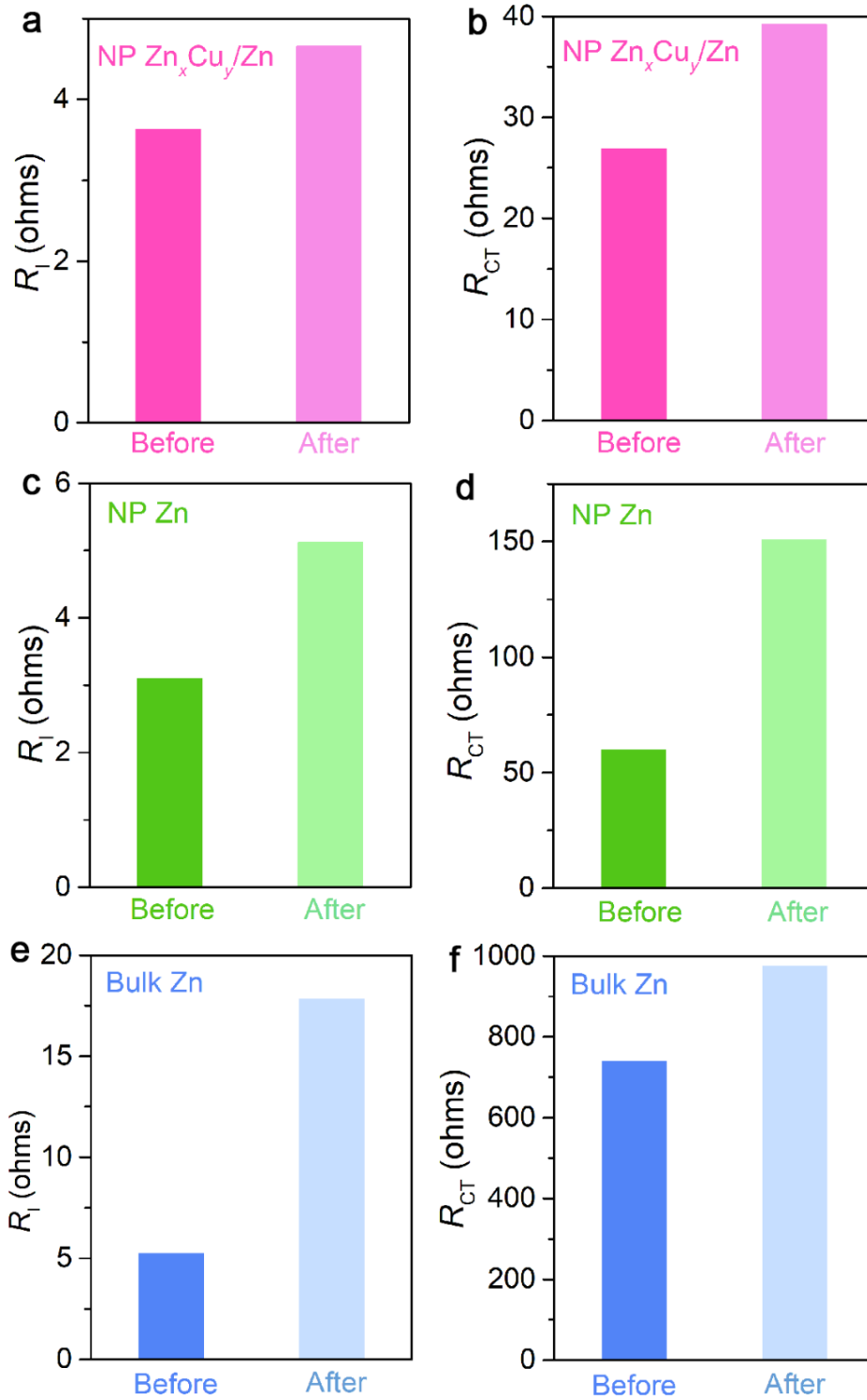


Fig. S16 (a, b) Comparison of R_I (a) and R_{CT} (b) values for nanoporous Zn_xCu_y/Zn electrodes before and after 100 cycles of Zn stripping/plating in their symmetric cells. (c, d) Comparison of R_I (c) and R_{CT} (d) values for nanoporous Zn electrodes before and after 100 cycles of Zn stripping/plating in their symmetric cell. (e, f) Comparison of R_I (e) and R_{CT} (f) values for bulk Zn electrodes before and after 100 cycles of Zn stripping/plating in their symmetric cells

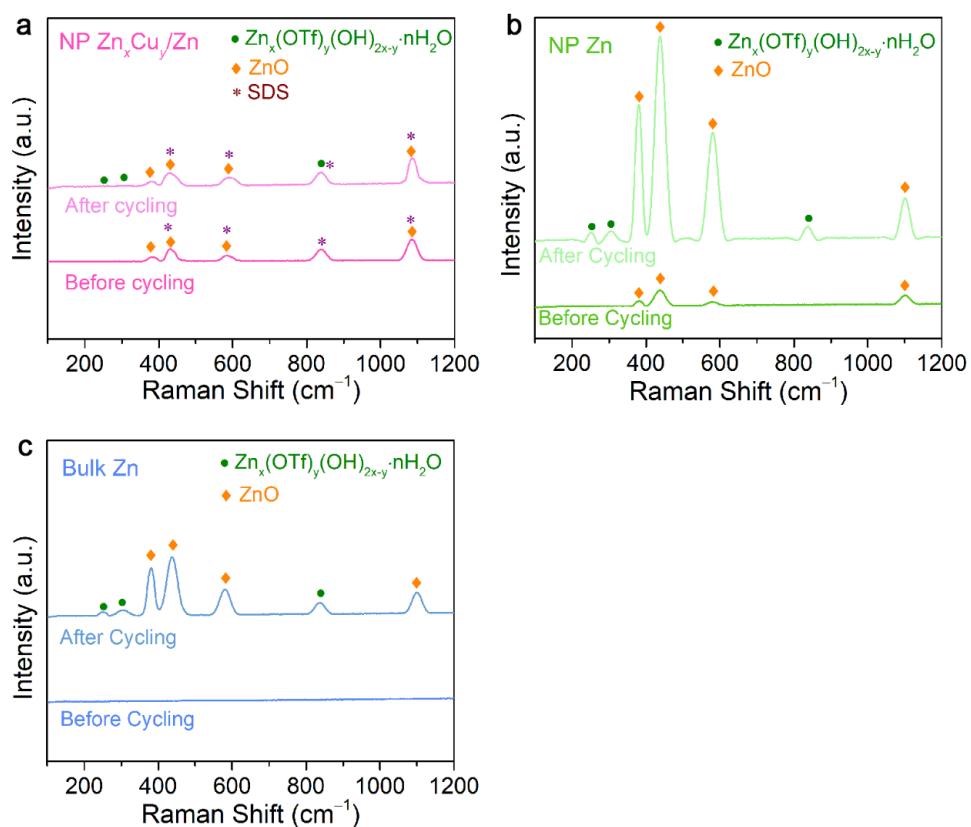


Fig. S17 (a-c) Raman spectra of nanoporous Zn_xCu_y/Zn (a), nanoporous Zn (b) and bulk Zn (c) before and after Zn stripping/plating for 100 cycles, during which there generate additional by-products of $Zn_x(OTf)_y(OH)_{2x-y} \cdot nH_2O$ and ZnO

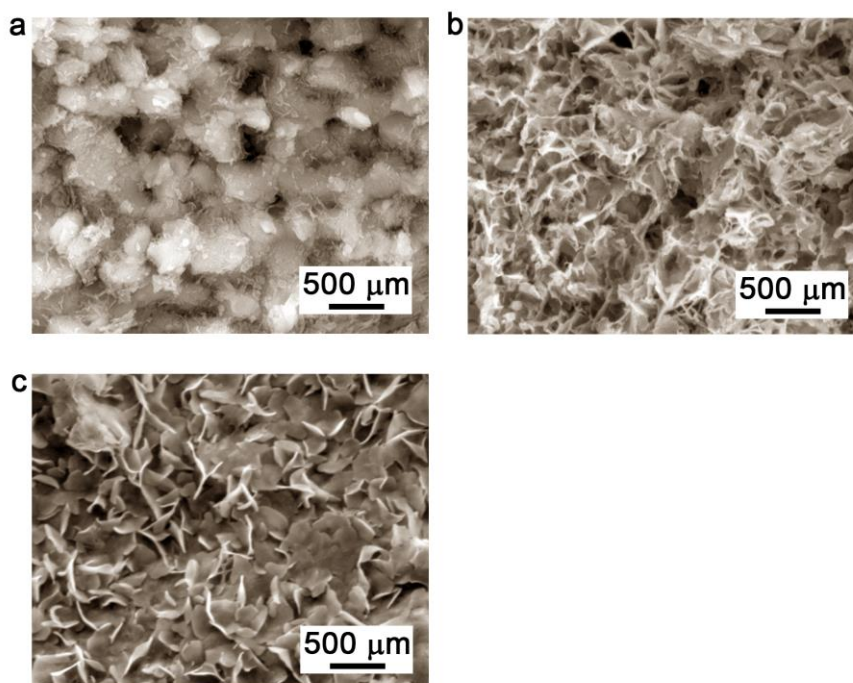


Fig. S18 (a) SEM image of nanoporous Zn_xCu_y/Zn electrode after Zn stripping/plating for 500 cycles (1000 hours). **(b)** SEM image of nanoporous Zn electrode after Zn stripping/plating for 150 cycles (300 hours). **(c)** SEM image of bulk Zn foil after Zn stripping/plating for 50 cycles (100 hours)

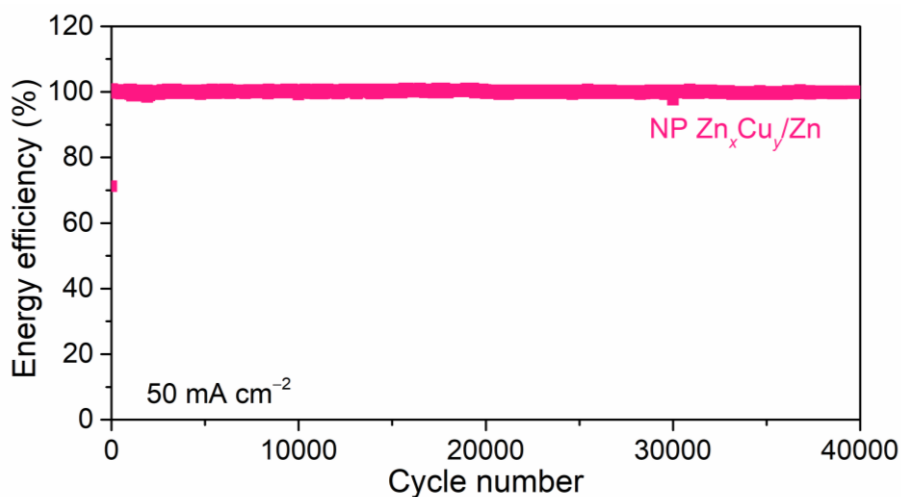


Fig. S19 Energy efficiency of nanoporous Zn_xCu_y/Zn electrodes during long-term cycling of Zn stripping/plating in 1 M $Zn(OTf)_2$ with 1 mM SDS at 50 mA cm^{-2}

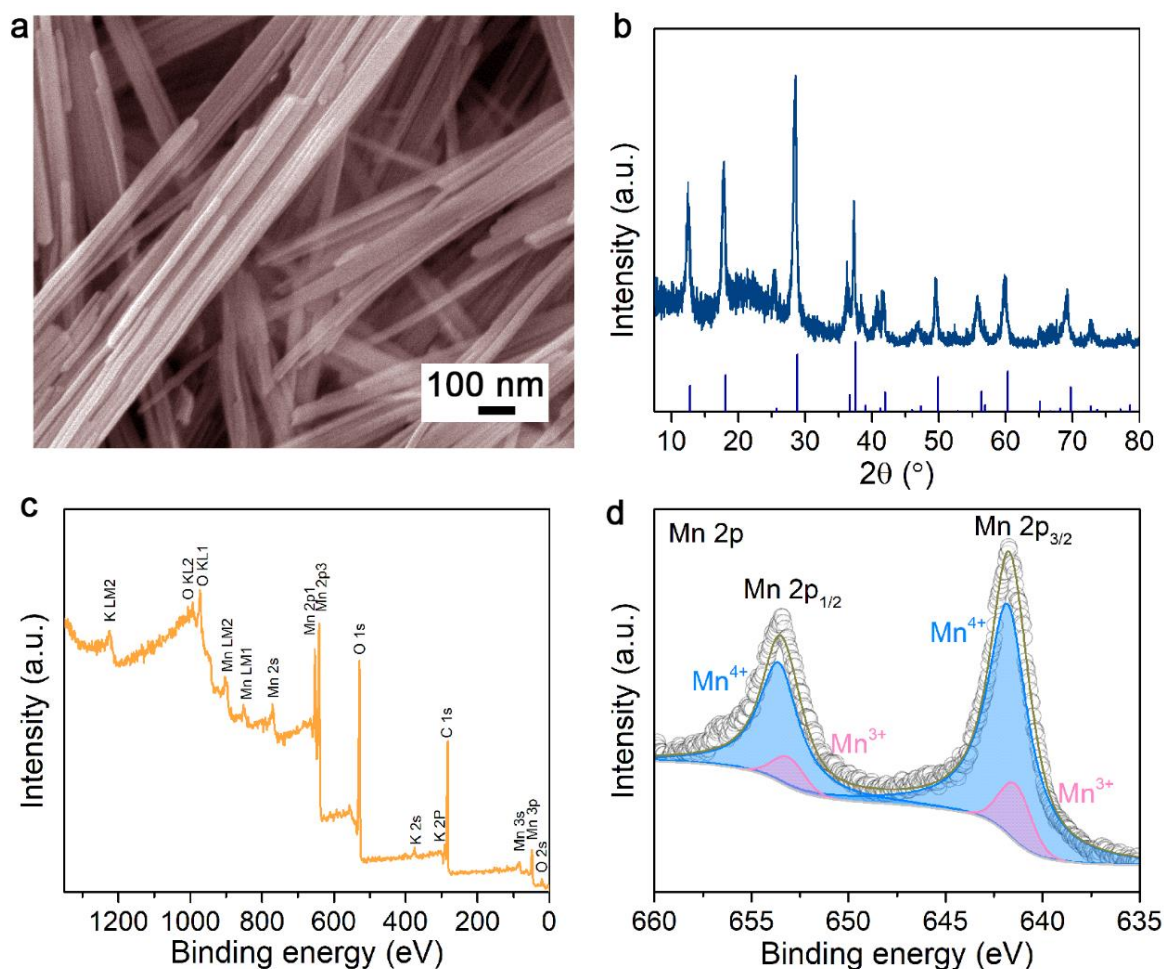


Fig. S20 Structural and chemical characterizations of K_zMnO_2 nanobelts. (a) Typical SEM image of as-prepared K_zMnO_2 nanobelts. (b) XRD patterns of K_zMnO_2 nanobelts. The line patterns show reference card 44-0141 for tetragonal phase of $\alpha\text{-MnO}_2$ according to JCPDS. (c) XPS survey spectrum of as-prepared K_zMnO_2 nanobelts, demonstrating the presence of preintercalated K^+ . (d) High-resolution Mn 2p XPS spectrum of K_zMnO_2 nanobelts

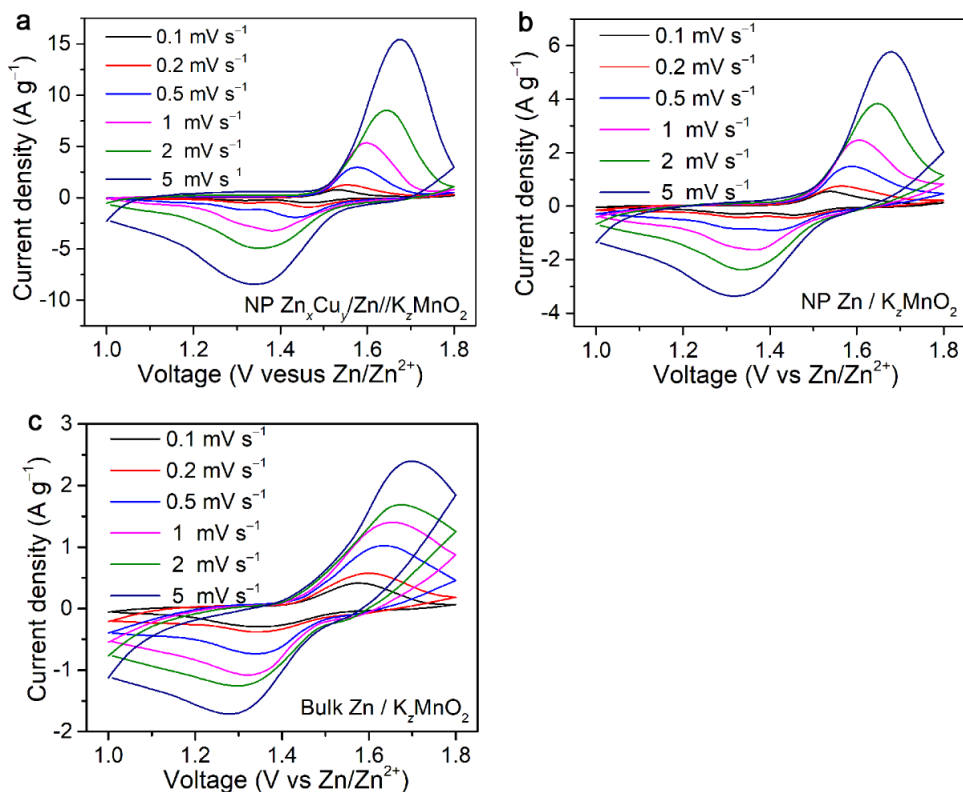


Fig. S21 (a-c) CV curves of full Zn-ion batteries of nanoporous Zn_xCu_y/Zn//K₂MnO₂ (a), nanoporous Zn//K₂MnO₂ (b) and bulk Zn//K₂MnO₂ (c) at various scan rates ranging from 0.1 to 5 mV s⁻¹

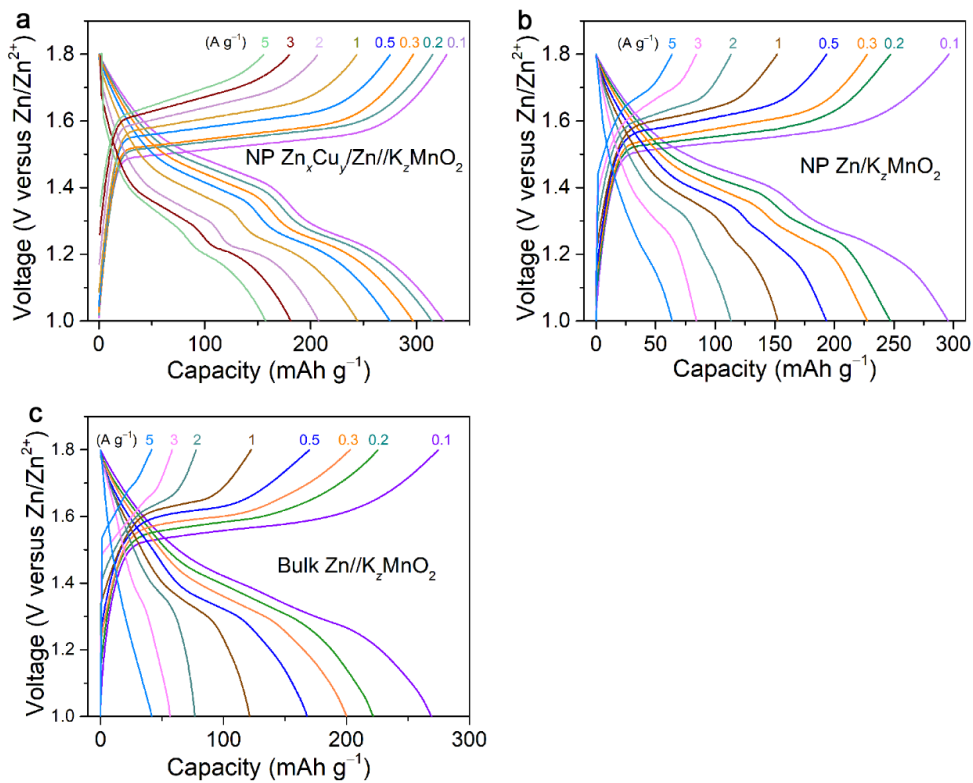


Fig. S22 (a-c) Voltage profiles of charge/discharge for full Zn-ion cells of nanoporous Zn_xCu_y/Zn//K₂MnO₂ (a), nanoporous Zn//K₂MnO₂ (b) and bulk Zn//K₂MnO₂ (c) at the specific currents ranging from 0.1 to 5 A g⁻¹. The applied specific current and the achieved specific capacity are calculated according to the loading mass of electroactive K₂MnO₂ in the cathode

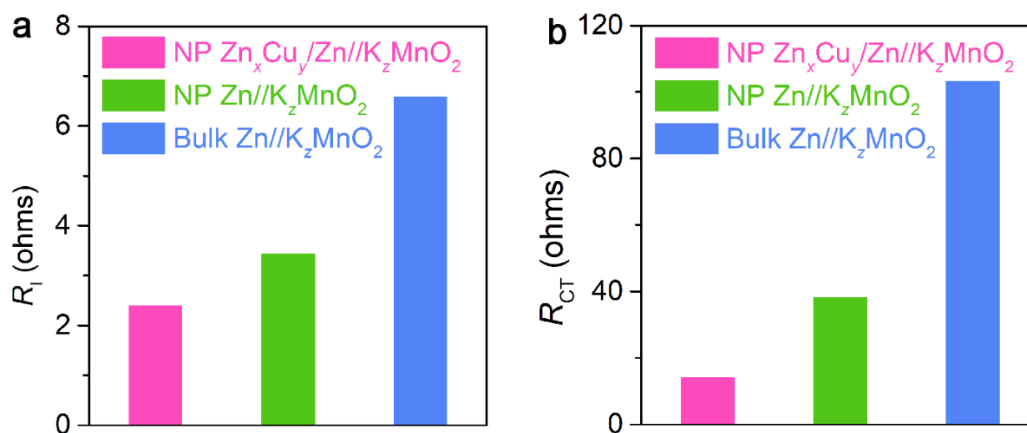


Fig. S23 (a,b) Comparison of R_1 (a) and R_{CT} (b) values for nanoporous Zn_xCu_y/Zn//K_zMnO₂, nanoporous Zn//K_zMnO₂ and bulk Zn//K_zMnO₂ AR-ZMB devices

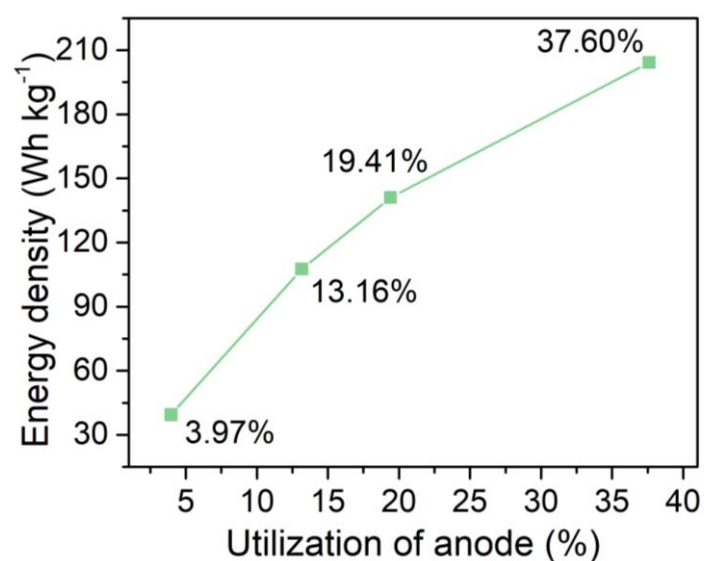


Fig. S24 Dependence of cell-level energy density on Zn utilization of anode in nanoporous Zn_xCu_y/Zn//K_zMnO₂ full cells

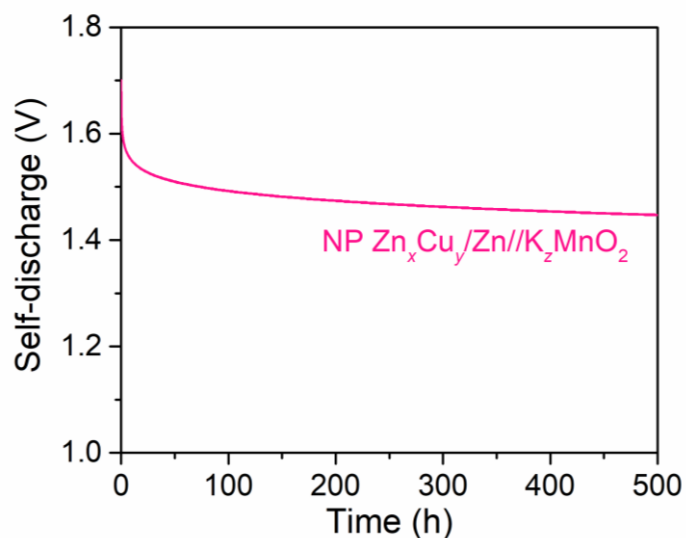


Fig. S25 Self-discharge profile for nanoporous Zn_xCu_y/Zn//K_zMnO₂ full cell

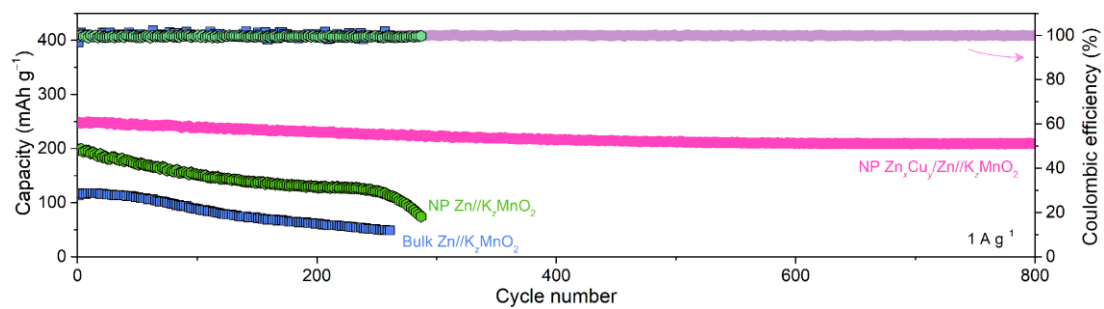


Fig. S26 Comparisons of capacity retentions and coulombic efficiencies for nanoporous $\text{Zn}_x\text{Cu}_y/\text{Zn}/\text{K}_z\text{MnO}_2$, nanoporous $\text{Zn}/\text{K}_z\text{MnO}_2$ and bulk $\text{Zn}/\text{K}_z\text{MnO}_2$ cells in a long-term charge/discharge cycling measurements at the specific current of 1 A g^{-1}